Applied Surface Science 517 (2020) 146185

Contents lists available at ScienceDirect

Applied Surface Science

journal homepage: www.elsevier.com/locate/apsusc

Full Length Article

Improvement of Ti/TiN interfacial shear strength by doping – A first principles density functional theory study

Abu Shama Mohammad Miraz[a], Eboni Williams[a], W.J. Meng[b], Bala R. Ramachandran[a], Collin D. Wick[a,*]

[a] College of Engineering & Science, Louisiana Tech University, Ruston, LA 71270, USA
[b] Mechanical & Industrial Engineering Dept., Louisiana State University, Baton Rouge, LA 70803, USA

ARTICLE INFO

Keywords:
Metal/ceramic interfaces
Doping
Nanocomposites
DFT
Charge density
Monte Carlo

ABSTRACT

The dependence of interfacial shear resistance on the substitutional doping of Al, V and Cr at the Ti/TiN interface was studied using first principles Density Functional Theory. Only Al dopants had negative enthalpies of mixing in Ti and at the Ti/TiN interface. Generalized stacking fault energies (GSFE) were calculated and their barriers were used as an estimate of shear resistance. The addition of Al increased the GSFE barriers of pure Ti when they were in adjacent atomic layers. It was found that when Al atoms were in contact, they had a destabilizing effect that led to the increased barriers in certain configurations. Near the Ti/TiN interface, the presence of one or two Al dopants increased the GSFE barrier by drawing some of the electron charge from the ceramic N atoms into the Ti phase. There was a general correlation between higher GSFE barriers and Al concentration at the Ti/TiN interface, which were attributed to both of the described effects: destabilizing Al-Al interactions and Al drawing electron density from the ceramic into the Ti phase.

1. Introduction

Metal/ceramic interfaces are frequently encountered in various engineering applications to improve the structural, electrical and magnetic properties of the constituent materials [1]. Many of these applications utilize metal/ceramic composites customized for a given service-environment by selectively combining the properties of the metal phase and the ceramic phase [2–4]. Ceramics have high hardness, thermal stability, and wear resistance that allow for their use in harsh environments involving high temperatures, pressures, and contact. Metals, on the other hand, are ductile with higher toughness. Metal/ceramic nanolaminates can possess high hardness and wear resistance along with enhanced toughness and ductility [5,6].

Many metal/ceramic combinations have been studied over the last few decades [7–21]. Physical and chemical vapor deposition–grown transition metal nitride coatings, such as TiN, have high hardness, low thermal conductivity, and may exhibit hardness increases as temperature increases due to isostructural compositional segregation (age-hardening) [22,23]. However, refractory ceramics, such as TiN, are brittle, allowing for deflection of cracks through the coating/substrate interface, leading to delamination and spallation [24]. Hence, metal interlayers, such as TiAl, Ti, and Ni, have been interdispersed with the ceramics, such as TiN and W_2N, to form multilayers in order to hinder crack propagation and crack deflection at interfaces [25–28]. Such property tailoring finds application related to gas turbines, aeroengines, automobile and aerospace components, machining and cutting tools, tribological contacts, etc. [2,29–36]. Strong adhesion and resistance to shear is desired for the above-mentioned applications to minimize wear and interfacial spallation. One way to improve these between the layers is to add a small amount alloying elements or 'dopants' to the system [37,38].

The influence of dopants has been reported for some of the metal/ceramic laminates such as Al/TiN [6,39], Al/TiC [40], Fe/Y_2O_3 [41], Fe/TiC [42], Ti/TiO_2 [43], Ni/Ni_3Al [44–46], Fe/TiN [47], Nb/Al_2O_3 [48], Mo/HfC [5], NiAl/Al_2O_3 [49,50], etc. Addition of Al to TiN resulted in higher hardness and friction co-efficient until the mole fraction of Al becomes higher than 0.6 in $Ti_{1-x}Al_xN$, after which the hardness and wear resistance are reduced [22,51,52]. Ti interlayers within the Ti/TiN multilayer nanolaminates were also alloyed with Al producing enhanced hardness and toughness [51,53]. A comparative study between bilayer Ti/TiN and TiAl/TiAlN deposited on austempered ductile iron (ADI) revealed that TiAl/TiAlN coatings had higher hardness and elastic moduli than Ti/TiN, although the critical load for the first delamination from scratch testing was higher for the latter [51].

* Corresponding author.
E-mail address: cwick@latech.edu (C.D. Wick).

https://doi.org/10.1016/j.apsusc.2020.146185
Received 5 November 2019; Received in revised form 13 February 2020; Accepted 21 March 2020
Available online 24 March 2020

For this particular study, it was stated that the TiAl/TiAlN system has more mismatch with ADI than Ti/TiN, which could be the reason for the lower critical load for the former.

Characterizing local interactions and geometries experimentally is difficult without disruption or deformation of the system being examined. At the same time, the increasing availability of high-performance computation allows first principles density functional theory (DFT) calculations to be performed for systems of moderate size and complexity. The neat Ti(0 0 0 1)/TiN(1 1 1) interface has been investigated with DFT calculations by some of the present authors, finding that basal slip tend to occur in the Ti layers adjacent to the interface, but not at the interface itself [54,55]. This was in agreement with molecular dynamics simulations and consistent with experimental observations [54].

To our knowledge, there are no studies of the effect of dopants on interfacial metal/ceramic shear strength. In this work, we probe the possibility of enhancing the adhesive properties of the Ti/TiN interfaces by adding Al, V or Cr dopants. The shear strengths of the systems are analyzed through adhesion and interfacial strength metrics such as work of adhesion and generalized stacking fault energy (GSFE)/γ-surface.

2. Methodology

2.1. Ti bulk and Ti/TiN interfaces

Generalized gradient approximation for the exchange–correlation functional proposed by Perdew, Burke and Ernzerhof (PBE) was used to perform ab-initio DFT calculations [56]. The valence electrons were represented by a plane wave basis set with a cutoff energy of 400 eV. The Projector Augmented Wave (PAW) pseudopotentials were used for core electrons as implemented in the Vienna Ab-Initio Simulation Package (VASP) package [57,58]. A 4 × 4 × 1 Γ–centered k-point mesh was used for the metal/ceramic systems with periodic boundary conditions [59]. No significant changes in the cell dimension or energy was observed with higher-level meshes and energy cutoffs. Spin polarized calculations were carried out to determine their impact on the geometry and the energetics of all the metal/ceramic combinations. For each, the structure and the enthalpy of mixing showed no significant impact from including spin polarized calculations, so it was not further considered in this study.

The simulations were setup similar to our previous work [55]. A total of 64 atoms (16 layers of 4 atoms) of Ti(0 0 0 1), along with 48 atoms of TiN(1 1 1) (6 layers of 8 atoms) were separately relaxed and brought in contact to create a single Ti(0 0 0 1)/TiN(1 1 1) interface aligned normal to the Z direction. Table 1 gives the unit dimensions and directions, parallel to the interface, for the two different phases. The final combination included 2 units in the X direction and 1 in the Y direction for both Ti and TiN. Before bringing Ti in contact with TiN, the Ti system was stretched in both the X and Y directions to match TiN. Since there are periodic boundaries, each phase had two interfaces, one metal/ceramic and one with vacuum, in which at least 15 Å of vacuum was present in the Z direction (see Fig. 1). The combined Ti/TiN system was then allowed to fully relax, and the resulting structure was used for the steps afterwards. This particular interfacial combination has been extensively studied experimentally [9,11,60,61].

The atomic layers and the planes in between them are denoted by M and P, respectively, as shown in Fig. 1. M = 1 is assigned to the atomic layer of Ti that is directly above the first N layer from the ceramic, and the plane between these two layers is designated as P = 0.

2.2. GSFE mapping

The GSFE or γ-surfaces in X and Y were calculated for planes at and near the interface (P = 0–3 in Fig. 1). Starting with the relaxed system, all atoms above a particular plane are displaced in the X and/or Y directions, keeping atoms below it fixed. After the displacements, only the Z positions of the atoms are allowed to relax. This is illustrated for the P = 0 plane in Fig. 2. For P = 1, an additional layer of 4 Ti atoms are fixed, with those above them translated, while for P = 2, there are two fixed Ti layers, etc. To generate the 2D GSFE surface plot, 10 equally spaced positions spanning the initial relaxed position to half the X cell length, along with 10 positions spanning half the Y cell length were taken. This allows a quadrant (half of both the X and Y cell lengths) to be sampled with 100 total positions. The energies of these positions are replicated once in both directions to generate the full 2D GSFE surface as shown, for example, in Fig. 2c and d for P = 0. When dopants are introduced into the system, the symmetry of the quadrants can be broken in certain situations, in which the entire X and/or Y directions need to be sampled, resulting in 200 total positions if one of the directions need to be fully sampled or 400 if they both do. Due to this increased computational burden, for the larger system size described in Section 3.2.2 (with 16 Ti atoms per layer), only the energy variation in the X dimension, [$\bar{1}$ $\bar{1}$ 2 0], was computed, allowing the atoms to relax in the Y and Z directions, with more details given below.

2.3. Doping configuration and stability

Pure Ti and the Ti/TiN systems were each doped with Al, Cr, and V, since these are common substitutional alloying elements of Ti [62,63]. The pure Ti system, which has two vacuum/Ti interfaces as shown in Fig. 1a, was initially tested to determine the influence of dopants on bulk GSFE and adhesion properties without the ceramic being present. To determine if the dopants created energetically stable systems, the enthalpies of mixing for the exchange of one and two dopant atoms (x = Al, Cr or V) with Ti atoms were calculated,

$$\mathrm{Ti}_{64} + n x_{\mathrm{bulk}} \rightarrow \mathrm{Ti}_{64-n} x_n + n \mathrm{Ti}_{\mathrm{bulk}} \quad (1)$$

where Ti_{64} represents the energy of the pure system shown in Fig. 1a, and bulk denotes the most stable crystalline systems for Ti or dopant. The positions of the Ti atoms that were exchanged with dopants were varied to find those near the GSFE slip plane with negative heats of mixing.

For the Ti/TiN systems, one and two dopant atoms were exchanged with different Ti atoms near the interface, and their heats of mixing were calculated:

$$\mathrm{Ti}_{88}\mathrm{N}_{24} + n x_{\mathrm{bulk}} \rightarrow \mathrm{Ti}_{88-n} x_n \mathrm{N}_{24} + n \mathrm{Ti}_{\mathrm{bulk}}. \quad (2)$$

When greater than two dopant atoms were exchanged with Ti atoms, the number of potential combinations was too large to systematically sample them. To overcome this challenge, a Monte Carlo approach as shown in Fig. 3 was used to find possible low energy configurations when four or more dopant atoms were examined.

Table 1
Crystal directions assigned as X and Y for Ti and TiN and their unit length along those directions.

Surfaces	Unit Directions		Unit Dimensions		Metal/Ceramic Periodic Units
	X	Y	X	Y	$(X \times Y)_{metal}/(X \times Y)_{ceramic}$
Ti(0 0 0 1)	[$\bar{1}$ $\bar{1}$ 2 0]	[1 $\bar{1}$ 0 0]	2.93	5.11	$(2 \times 1)_{Ti}/(2 \times 1)_{TiN}$
TiN(1 1 1)	[1 $\bar{1}$ 0]	[1 1 $\bar{2}$]	3.01	5.22	

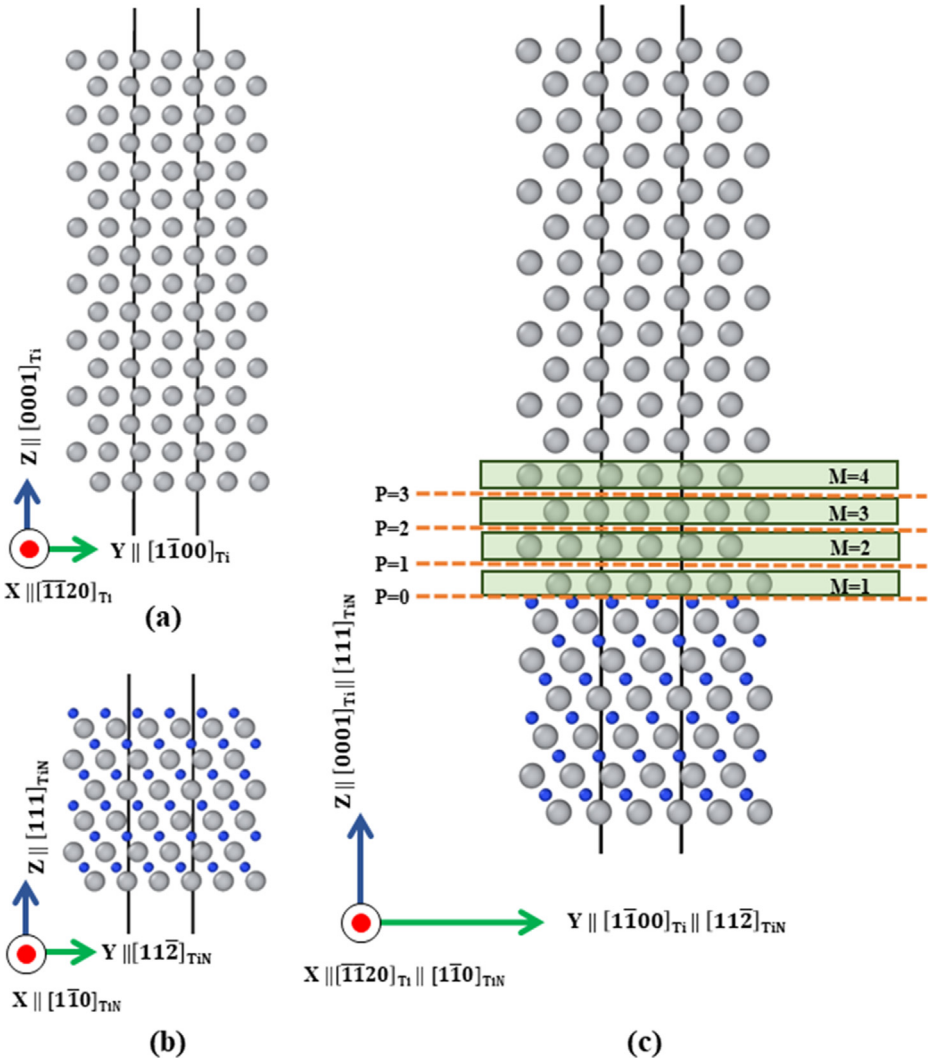

Fig. 1. Structures of (a) Ti(0 0 0 1) and (b) TiN(1 1 1) with the vertical black lines indicating the boundaries of the simulation cell. (c) Ti(0 0 0 1)/TiN(1 1 1) structure, atomic layers near the interface in the green shaded boxes are denoted by M and the planes between the layers marked with broken lines are denoted by P.

For the first step of the Monte Carlo procedure, 4, 8, or 16 randomly chosen Ti atoms are replaced with Al atoms. These include the 64 atoms in the Ti phase, along with the 24 atoms in the TiN phase. However, the two layers closest to the vacuum for both the Ti and TiN phases were not included in this, as solid/vacuum interfaces are not the focus of this investigation. The atomic positions are then relaxed utilizing DFT calculations, keeping the cell dimensions the same as the non-doped system. For each step, 4 trials ($T = 4$) are performed, in which each trial swapped two random Al atoms with two random Ti atoms (excluding those in the two layers closest to the vacuum for both phases), followed by full relaxation of all atomic positions. The trial with the lowest energy calculated from DFT is then identified, and if it is less than the energy of the previous configuration plus an energy tolerance ($\delta = 0.1$ eV in this work), it is chosen as the new one. The purpose of the energy tolerance is to keep the system from being stuck in local minima. If during any trial relaxation, the VASP calculation fails to converge, the trial is discarded. To ensure that the algorithm is reasonably ergodic, two random initial configurations were chosen for a system and the Monte Carlo procedure run on them to check if they converge to similar energies. For each procedure, 50 Monte Carlo steps (N) were carried out.

3. Results and discussion

3.1. Bulk Ti doping

3.1.1. Enthalpies of mixing for different dopants

The enthalpies of mixing (ΔH_{mix}) for the doping of the Ti bulk system, which consisted of 64 atoms, with single Al, Cr, and V atoms are shown in Table 2. The only dopant atom with a negative enthalpy of mixing is Al, while Cr and V have significant positive enthalpies. The positive enthalpies signify that the configurations with Cr and V are unlikely to form stable structures. Therefore, only Al was considered for further study as a dopant in Ti for this work. The ΔH_{mix} for adding a second Al dopant to the Ti bulk system was calculated with two dopants in the same layer (1,1), and in different layers (1,2). Both have negative enthalpies, while the (1,2) system has the lowest overall. For HCP Ti having 4 atoms per layer, two dopants in the same layer can assume only one unique nearest–neighbor position with respect to each other. Dopants in two consecutive layers, such as in the (1,2) systems, can reside in two unique nearest-neighbor positions: one where the Al atoms are 1st nearest neighbors, and another where the Al atoms are 2nd nearest neighbors (See Fig. S1(b) in supplemental materials). The system in which the Al atoms are in the 1st nearest neighbor position has an energy of −1.05 eV, which is significantly higher than the 2nd nearest neighbor energy shown in Table 2.

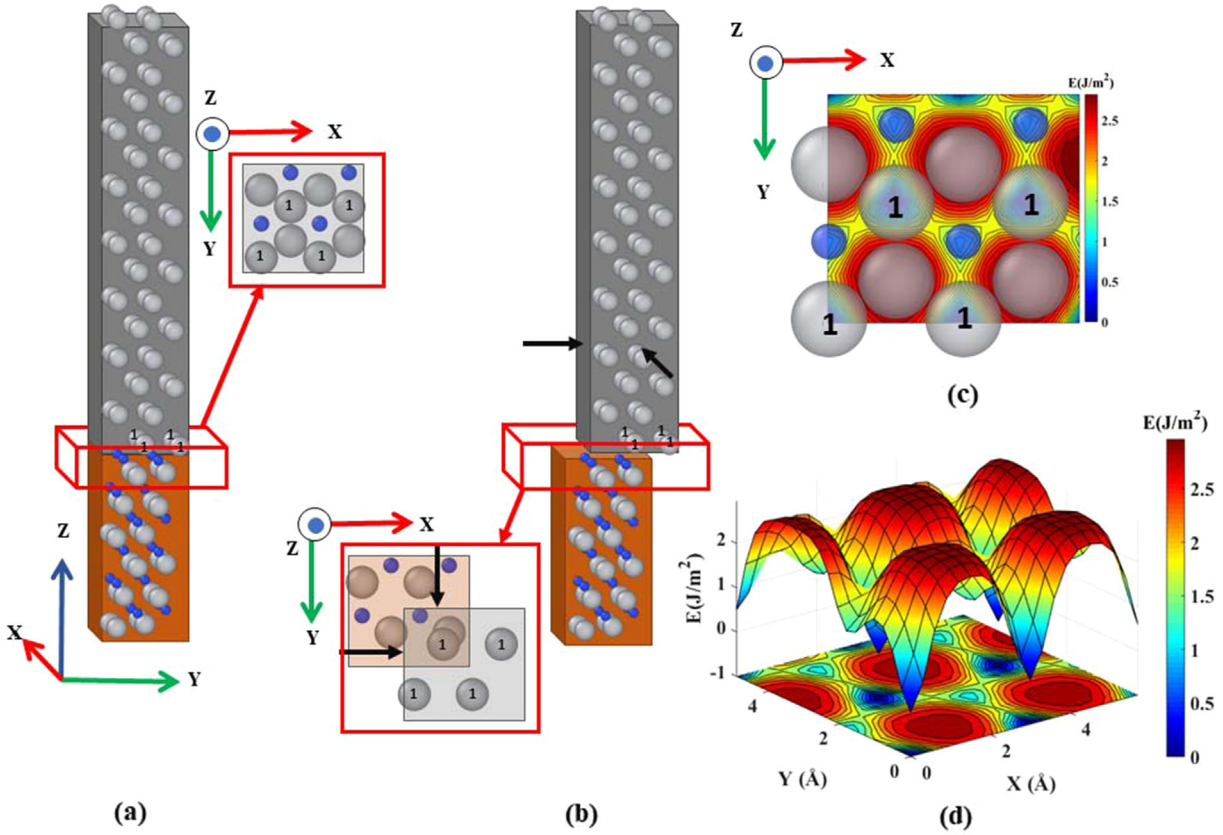

Fig. 2. Snapshots of the Ti/TiN system with Ti and TiN-phases marked by grey and brown shades, respectively for (a) the fully relaxed system, and (b) the displaced system. The atoms marked with '1' reside at M = 1 layer, and the snapshots facing the z direction show the atomic layers adjacent to the displacement plane (P = 0). (c) The P = 0 2D GSFE surface with the relaxed atomic positions of the M = 1 and the first two atomic layers in the ceramic present. (d) 3-dimensional visualization of the GSFE surface. (Color print required).

3.1.2. GSFE surfaces and barriers to shear displacement

From here on, the notation $S^{b\ or\ i}_{\{M=(m,n)\}}$ will be used to refer to the Al-doped system [superscript *b* for bulk Ti and *i* for Ti/TiN], where one Al atom is in the M = *m* layer and the other at the M = *n* layer. For a single atom at M = *m*, the notation is $S^{b\ or\ i}_{\{M=(m)\}}$. For Ti/TiN systems, the locations of the different M layers are shown in Fig. 1c, while for bulk Ti, they are shown in Fig. 4a.

To examine the effect of substitutional Al atoms in the HCP Ti matrix, 2D GSFE surface calculations were carried out for the doped systems as shown in Fig. 4. The 2D GSFE surface of pure Ti bulk is shown alongside the GSFE surface of $S^{b}_{(1)}$ in Fig. 4d and e, respectively. The minimum energy paths on these surfaces can be traced as shown in these figures and is plotted as a function of X in Fig. 4f along with those of $S^{b}_{(1,2)}$ and $S^{b}_{(1,1)}$. The symmetry of the GSFE planes allows for a periodic variation in the minimum energy path along X for most systems. Thus, the minimum energy path is plotted until it reaches a point from which it repeats itself. The $S^{b}_{(1,2)}$ system requires 6 Å of displacement until periodicity is achieved. The highest GSFE barrier can be extracted from this, which is used to compare the different systems studied. Higher GSFE barriers should coincide with higher resistance to shear. There is a small decrease of 0.013 J/m^2 in the barrier height with the exchange of a single Al atom from that of the pure bulk as seen in Fig. 4f. For all the systems studied, the only one with increased barrier height was the $S^{b}_{(1,2)}$ system at its P = 1 plane. As can be observed in Fig. 4b, this plane separates two layers, each with one Al atom.

After an approximate 1.5 Å displacement along the X direction (see Fig. 4f), the configurations for bulk Ti corresponds to local FCC stacking. The difference in energy between this local FCC stacking configuration and the global minimum energy, which is HCP stacking, gives the stacking fault energy (SFE). One may expect that a higher SFE energy corresponds to higher GSFE barriers. To verify this, they are plotted against one another in Fig. 4g. There is indeed a correlation between these two. In particular, the SFE for the $S^{b}_{(1,2)}$ system is considerably higher than that of the pure Ti, and it is the only system with an increased GSFE barrier upon doping. This suggests that destabilizing the FCC configuration with respect to the HCP configuration may be a good strategy for increasing the barriers to shear.

Snapshots from the M = 1 and M = 2 layers of the $S^{b}_{(1,2)}$ system viewed from Z direction are given in Fig. 5b. HCP_1 corresponds to the minimum energy configuration at X = 0 Å, while FCC and HCP_2 correspond to the configurations at X = 1.5 Å and X = 3 Å, respectively, as indicated with red arrows in the minimum energy path in Fig. 5b. The HCP_2 configuration, which would be identical to the HCP_1 configuration for the undoped system, is higher in energy than HCP_1 for $S^{b}_{(1,2)}$. What the HCP_2 and FCC configurations share that the HCP_1 configuration does not is that the Al atoms are nearest neighbors. When Al atoms are in adjacent layers, configurations in which Al atoms are 1st nearest neighbors are destabilized with respect to those in which they are not. This conforms to the results obtained from the energy of mixing calculations described in Section 3.1.1, where a dopant atom in the 1st nearest neighbor position of another dopant atom resulted in a higher energy than if it was placed in the 2nd nearest neighbor position. This destabilizing effect results in an increase in GSFE barriers for transitions from HCP_1 to HCP_2 configurations.

3.2. Low concentration doping of interfaces

3.2.1. Enthalpies of mixing

The substitutional dopant atoms were added at the M = 1, 2, 3 and 4 layers of the Ti/TiN interface (see Fig. 1c) as described in Section 2.3.

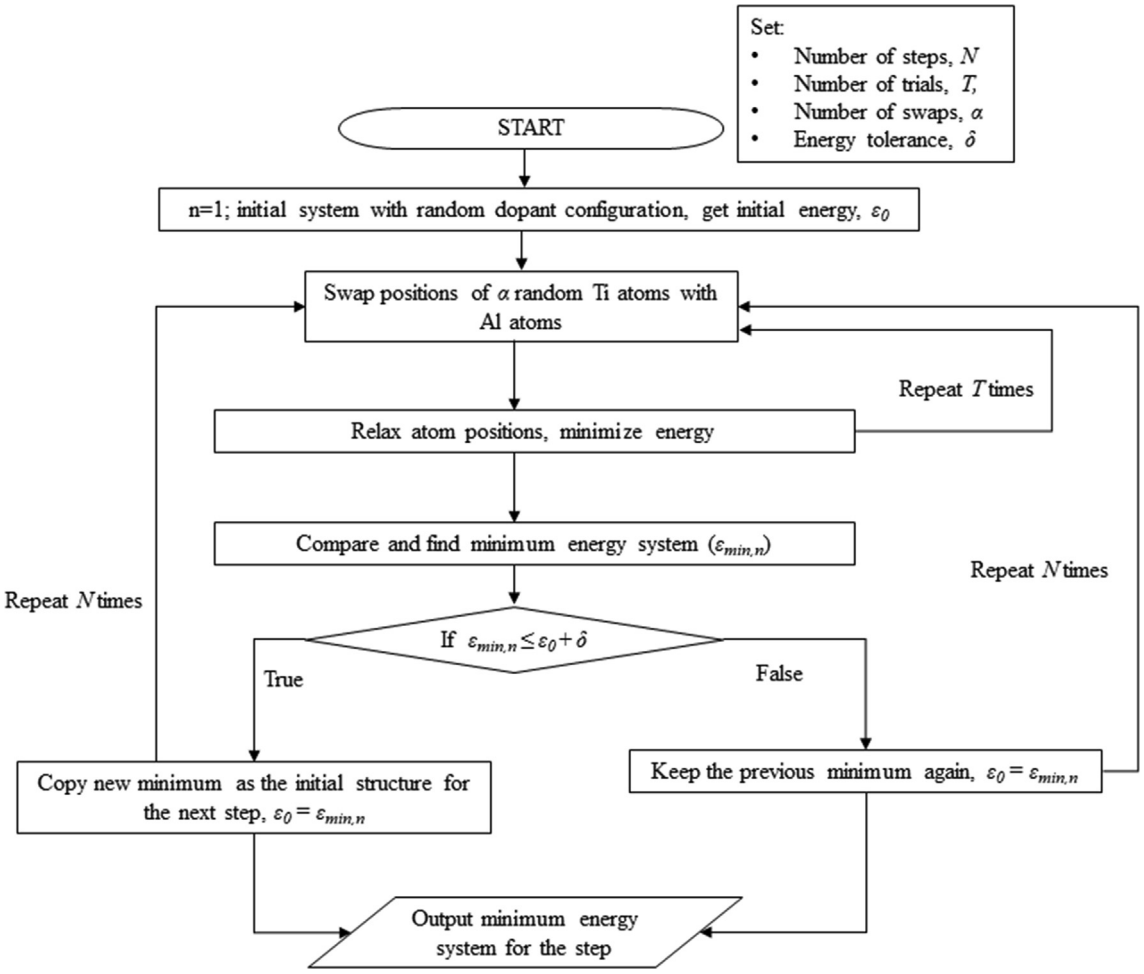

Fig. 3. Flow chart of the Monte Carlo procedure.

Table 2
Enthalpies of mixing for the doping of bulk Ti. (1,1) indicates atoms in the same atomic layer, and (1,2) indicates them in two separate layers.

Dopants	Layer(s) of Dopant Location	$\Delta_{mix}H$ (eV/atom)
Al	(1)	−0.94
	(1,2)	−1.99
	(1,1)	− 1.54
Cr	(1)	0.97
V	(1)	4.38

The resulting ΔH_{mix} are listed in Table 3. As mentioned earlier, the ΔH_{mix} values were calculated from Eq. (2). Cr and V doping results in significantly positive enthalpies for all combinations studied. This further signifies that they are unlikely to form stable structures with Ti in the system size studied, so they are not studied further in this work. One Al atom in the M = 1 layer results in positive enthalpies, while one Al atom in M > 1 results in negative enthalpies of similar magnitude as in bulk Ti. Negative enthalpies similar to the bulk Ti are observed for M > 1 when two dopants are present, with more negative enthalpies for dopants in separate layers. As with single dopants, substitution of one Al in M = 1 yields positive enthalpies as evident from the (2,1) entry in Table 3. For systems with two dopants, such as (2,2), (2,3) and (2,4), the possible nearest neighbor positions are explored in a similar manner as for bulk Ti (explained in Section 3.1.1) and the most energetically favorable system is listed in Table 3. In general, when the Al atoms are 1st nearest neighbors, they are less stable than when 2nd nearest neighbors.

3.2.2. GSFE surfaces and minimum energy paths

The 2D GSFE surfaces of the (0 0 0 1) planes (P = 0–3) near the interface for undoped Ti/TiN systems were calculated, and also for single dopants in the M = 2 and 3 layers (M = 1 is not shown due to the fact that it has a positive enthalpy of mixing). The minimum energy paths along the 2D GSFE surfaces for these as a function of X, along with that for bulk Ti are shown in Fig. 6. As in previous work, the lowest GSFE barrier for Ti/TiN is present in the P = 1 plane of the system (see Fig. 6a) [64]. The addition of a single dopant atom adjacent to the P = 1 plane (i.e. in M = 2), significantly increases the barrier for shear, by more than two times (see Fig. 6b). Even with the significant increase, the barrier is only around half as much as that in bulk Ti. The minimum energy paths were also calculated for cases with 2 dopant atoms present, which shows that the $S^{i}_{(2,2)}$ system had the highest barrier height of all the possible combinations, which is still below that of bulk Ti. The GSFE surfaces and the minimum energy paths for P = 1 plane of these systems are provided in the supplementary document in Figs. S2 and S3.

For the P = 1 case, the local FCC configuration is stabilized with respect to HCP for the undoped Ti/TiN system, which can be seen by the much lower energy of the local minimum at X = 1.5 Å for P = 1 in comparison with Pure Ti in Fig. 6b. Substituting a single Al atom in the M = 2 layer ($S^{i}_{(2)}$) does not significantly change the FCC and HCP energies *despite the fact that it significantly increases* the GSFE barrier. This points to a different cause for the increase in GSFE barriers than in bulk Ti. A plausible hypothesis is that the presence of electronegative N atoms in the ceramic attracts electron density from the interfacial Ti atoms towards the ceramic bulk. This results in the region in the P = 1

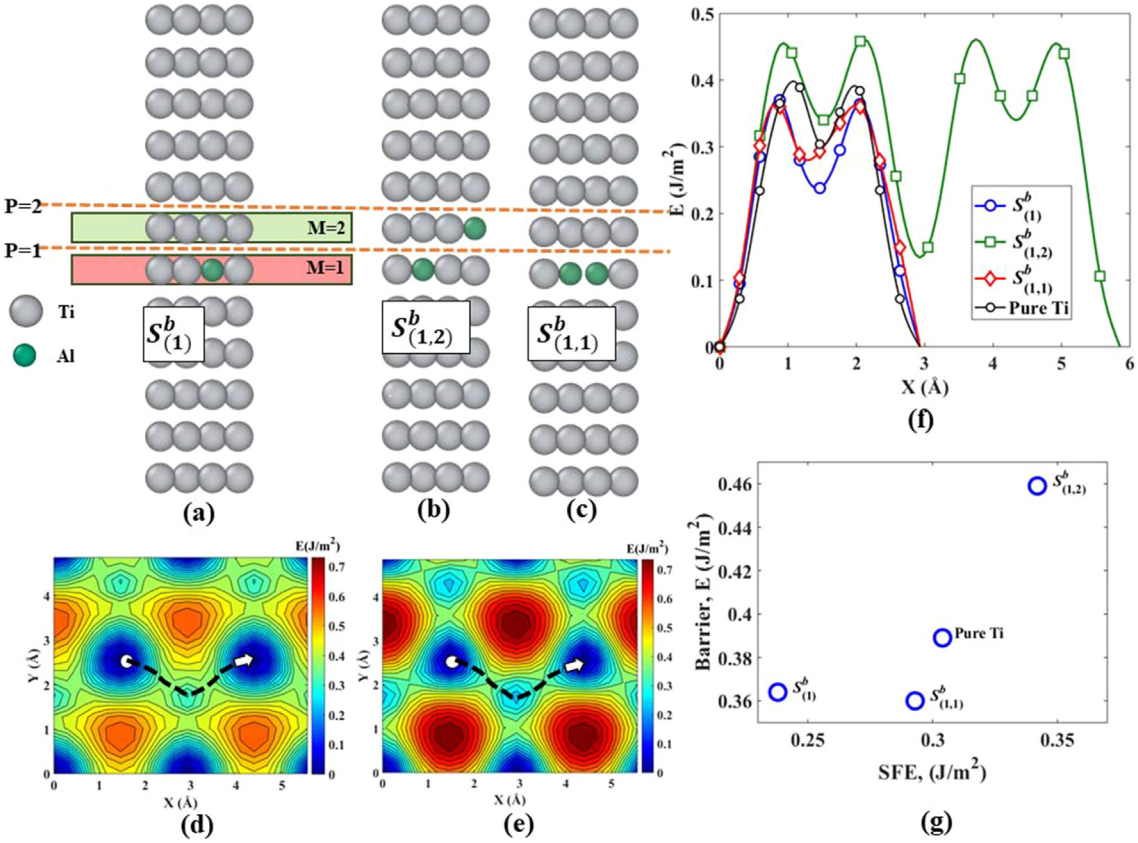

Fig. 4. Snapshots of (a) $S^b_{(1)}$, (b) $S^b_{(1,2)}$ and (c) $S^b_{(1,1)}$. 2D GSFE of (d) pure Ti and (e) $S^b_{(1)}$. (f) Plot of minimum energy path of pure bulk Ti, $S^b_{(1)}$, $S^b_{(1,2)}$ and $S^b_{(1,1)}$ along the X||[$\bar{1}$ 1$\bar{}$ 2 0] direction. (g) GSFE barrier heights of the pure Ti, $S^b_{(1)}$, $S^b_{(1,1)}$and $S^b_{(1,2)}$ systems plotted against the Stacking fault Energy (SFE) of the same systems. (Color print required).

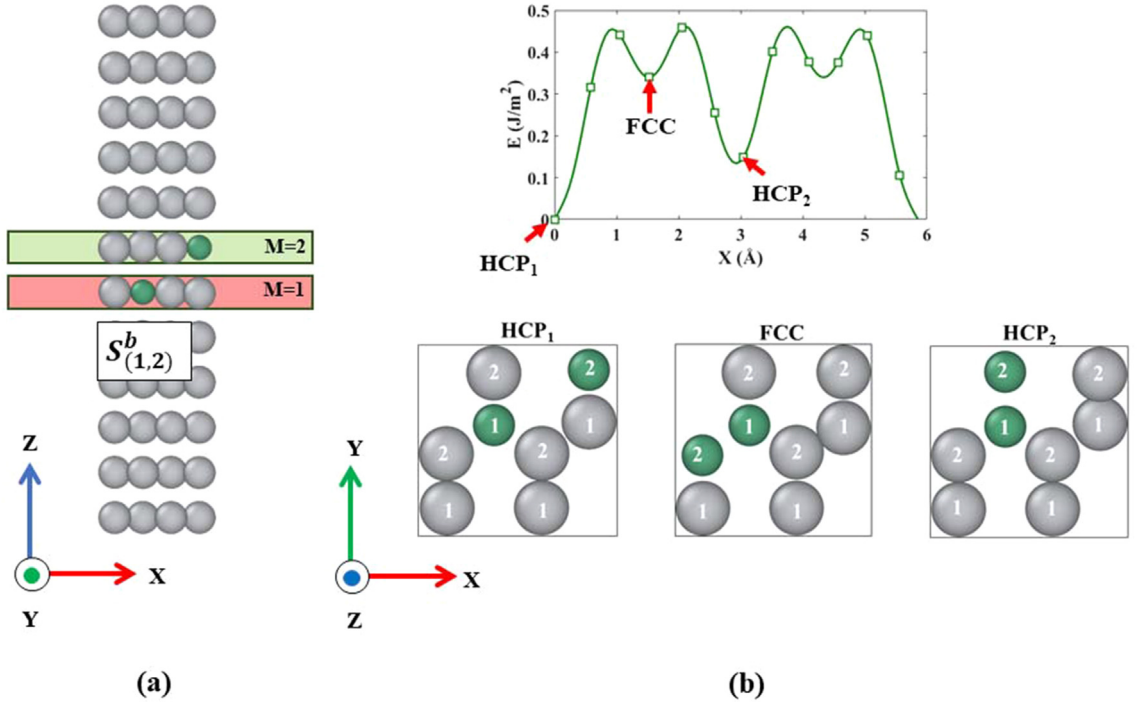

Fig. 5. (a) $S^b_{(1,2)}$system (b) Snapshots of the M = 1 and M = 2 layers viewed form the Z direction for different configurations formed along the minimum energy path.

Table 3
Enthalpy of mixing for the doping of Ti/TiN. The locations correspond to M shown in Fig. 1c.

Dopants	Layer(s) of Dopant Location	ΔH_{mix} (eV/atom)
Al	(1)	1.17
	(2)	−1.07
	(2,1)	0.38
	(2,2)	−1.92
	(2,3)	−2.04
	(2,4)	−1.99
	(3)	−0.87
	(3,3)	−1.45
Cr	(1)	1.41
	(2)	0.91
	(3)	0.94
V	(1)	0.65
	(2)	0.51
	(3)	0.51

plane (see Fig. 1c) to have reduced electron density as has been pointed out by us previously [55]. Another consequence of this will be that Ti atoms in the M = 1 layer will carry a net positive charge. To test this hypothesis, Bader charge analysis was performed on the Ti/TiN systems [65,66].

The average charge as a function of Ti atomic layer (M in Fig. 1c) position for different systems near the Ti/TiN interface is plotted in Fig. 6c. The metal layers in the TiN phase are numbered with negative integers, starting with −1 for the layer closest to the interface. In the ceramic, the electronegative N atoms carry a significant negative charge, while the Ti atoms have an equally positive charge. As described, the M = 1 layer is positively charged in all cases. The M = 2 layer has a slightly positive charge for the undoped system, showing that the electronegative N layer significantly impacts the charges of at least two layers in the Ti-phase. This would be expected to weaken the interactions between these two layers, causing a decrease in the GSFE barrier. Incorporating Al atoms, which are slightly more electronegative than Ti atoms [67], decreases the average charge in the M = 2 layer. The Al Bader charge in this layer is close to −1.0*e*, while the Ti charges (in the M = 2 layer) range between 0.1*e* and 0.3*e*. As a consequence, the purely electrostatic interaction between these M = 2 Al atoms and the positively charged Ti atoms in the M = l layer will be more attractive than between Ti atoms. This should increase the interaction between the M = 1 and M = 2 layers, and thus also increase the GSFE barriers. Accordingly, the barrier height is expected to be even higher with more Al atoms present at the M = 2 layer. This is consistent with the results as the $S^i_{(2,2)}$ system has the highest GSFE barrier.

While the systems with one Al atom have an overall low Al concentration, the concentration in the particular layer they are present is still 25%, since there are only four atoms in each layer. To investigate system size effects, a calculation that has twice the size in the X and Y directions were examined. This system consisted of 8 layers of 16 atoms, resulting in each layer having four times as many atoms as the previous calculations. With a single Al atom present, only 6.25% of the atoms in that layer are dopants. As with the smaller systems, $S^i_{(1)}$ was not energetically favorable whereas both $S^i_{(2)}$ and $S^i_{(3)}$ had negative ΔH_{mix}. Due to the increased size of these calculations, the 2D GSFE

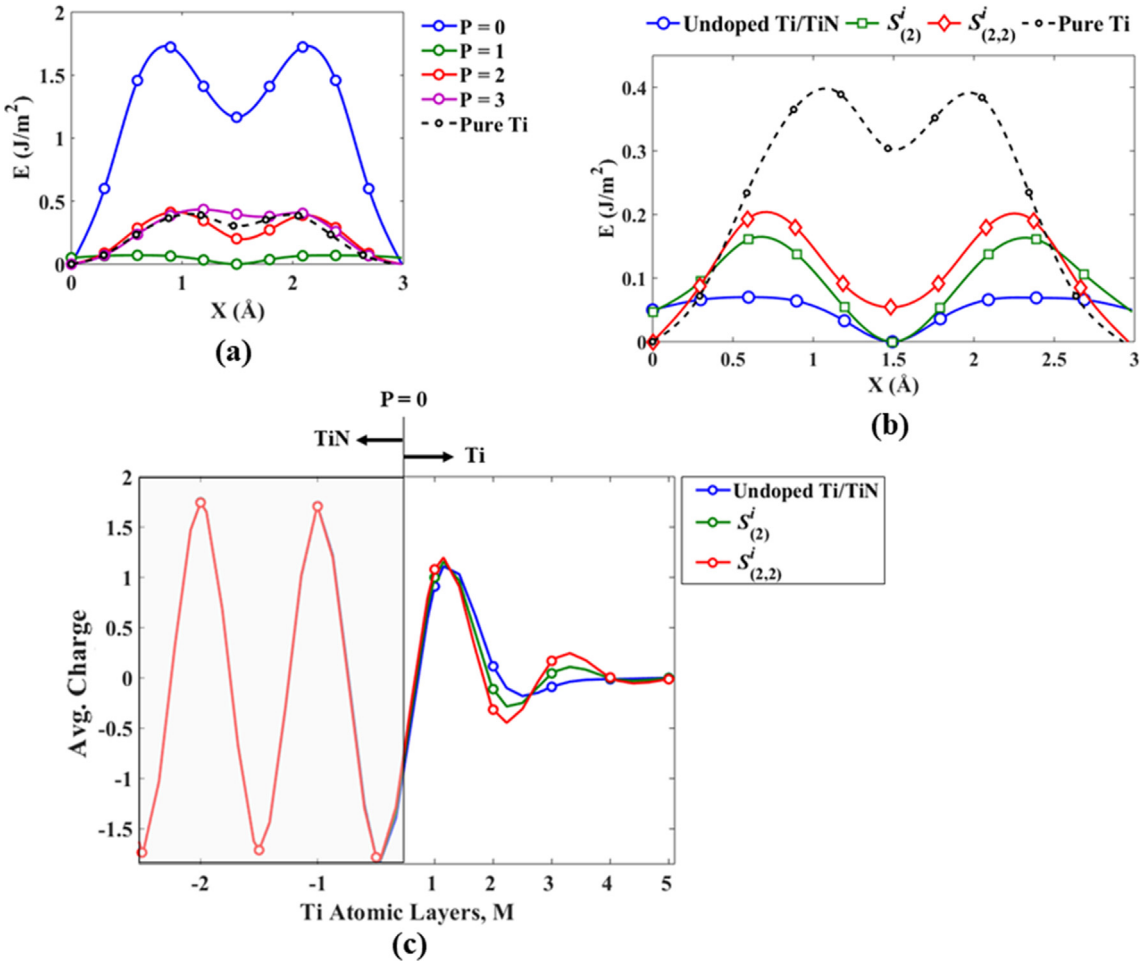

Fig. 6. (a) Minimum energy path for pure bulk Ti and the P = 0–3 planes of undoped Ti/TiN. (b) Comparison for P = 1 of undoped Ti/TiN, $S^i_{(2)}$, and $S^i_{(2,2)}$ with pure bulk Ti. (c) Average Bader charge per atom for each Ti atomic layer. (Color print required).

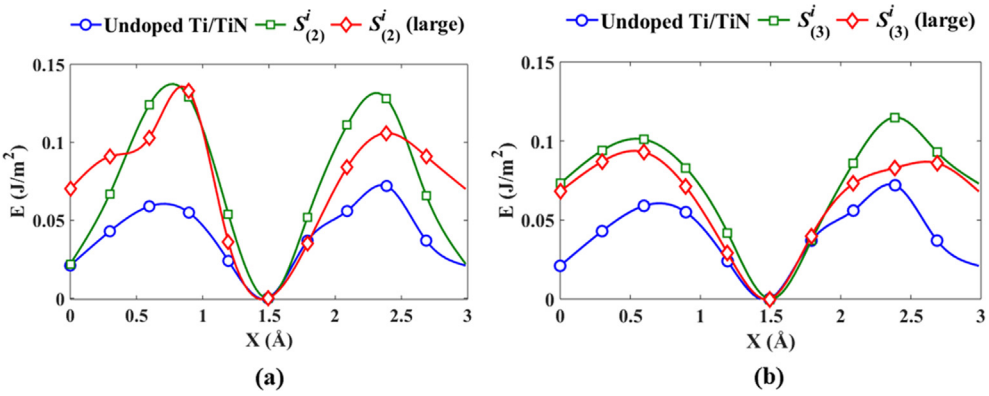

Fig. 7. (a) P = 1 GSFE comparisons of undoped Ti/TiN with (a) $S^i_{(2)}$ and larger system of $S^i_{(2)}$, (b) $S^i_{(3)}$ and larger system of $S^i_{(3)}$. (Color print required).

surface calculations were computationally too expensive to carry out. To simplify these calculations, while allowing direct comparisons with the smaller systems to be made, the 1D GSFE in the X direction was computed, allowing both the Y and Z positions to relax. The results can then be compared with the variation of energy along the analogous paths in the smaller systems.

This comparison of the 1D GSFE in the X direction for the larger system with the analogous path on the 2D GSFE surface for the smaller systems is presented in Fig. 7. The largest difference between the smaller and larger systems is the asymmetric nature of the GSFE plots. However, the energy barriers are of similar magnitude between the two albeit with subtle differences. For instance, the $S^i_{(2)}$ system's GSFE barrier is almost identical between the largest and smallest system, while for the $S^i_{(3)}$ system, the larger system has only a slightly lower barrier than the smaller one. This shows that at even lower dopant concentrations, significant increases in barrier height of the weakest GSFE plane (P = 1) can be obtained.

3.3. Higher concentration doping

3.3.1. Creation of low energy configurations

The Monte Carlo procedure described in Section 2.3 was utilized to find low energy configurations of the doped systems with 4, 8, and 16 Al atoms among all the Ti atoms in the Ti/TiN system, excluding the two layers closest to the vacuum for both phases. For each of these systems, two initial configurations were generated to determine if the Monte Carlo procedure generated similar final structures. Fig. 8a and b shows the energy versus step number for the Monte Carlo procedure for the system with 8 and 16 Al atoms present respectively, while the results for the systems with 4 atoms are given in Fig. S4 in the supporting information. As is apparent from the figures, the energies converge to similar values within the 50 Monte Carlo steps for the three systems. Fig. 8c also shows a representative snapshot of the systems with 4, 8, and 16 Al atoms. The Al atoms do not cluster together to a significant degree but remain rather dispersed. Moreover, Al atoms are rarely present in the TiN phase or in the M = 1 layer, which is expected since AlN has a different crystal structure than TiN. The overall ΔH_{mix} for the

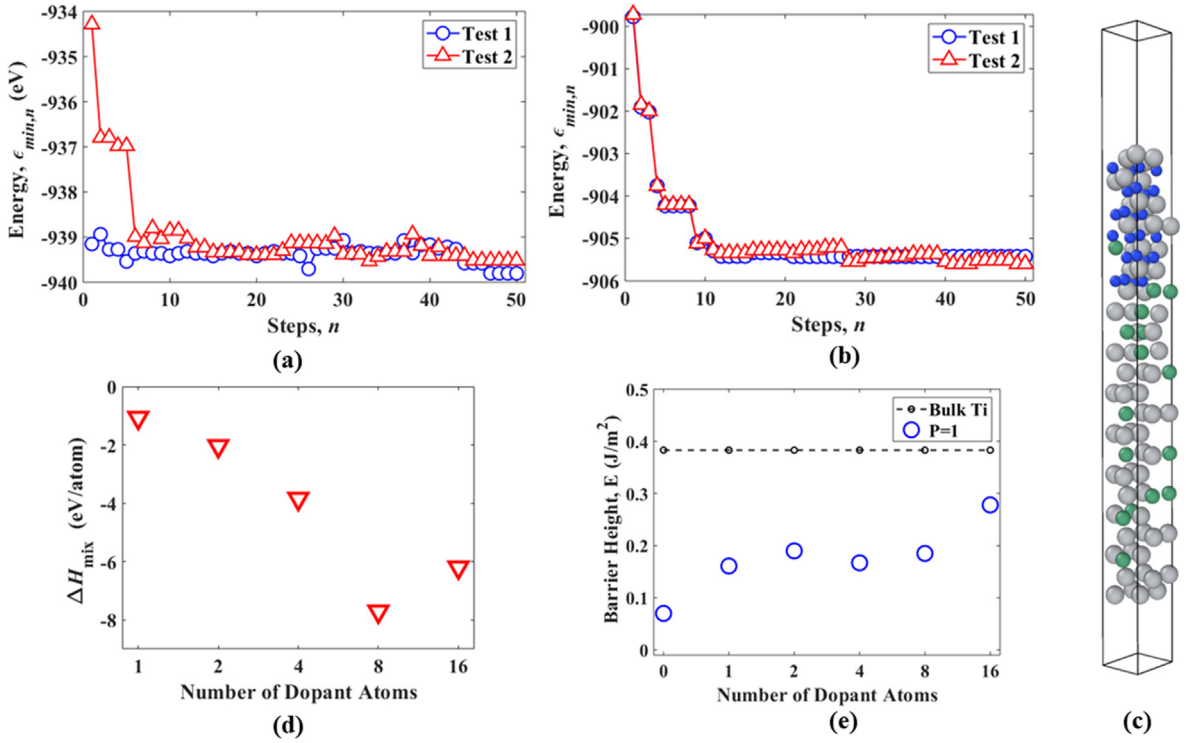

Fig. 8. Energy vs. step in the Monte Carlo minimization scheme with (a) 8 Al and (b) 16 Al atoms. (c) Snapshot of the system with 16 Al atoms. (d) Enthalpy of mixing as a function of the number of Al atoms. (e) GSFE barrier height for P = 1 as a function of composition.

different systems were calculated using Eq. (2) and are shown in Fig. 8d. The ΔH_{mix} is most negative for the system with 8 atoms, but there is a negative enthalpy for all of the systems studied. The system with 16 Al atoms is consistent with Ti_3Al, which is a known alloy [68,69].

The P = 1 plane 2D GSFE surfaces were calculated for the lowest energy configurations found for each of these systems, and the minimum energy paths were identified. Only the P = 1 planes are shown due to the fact that they had the lowest barriers for the Ti/TiN system. The 2D GSFE results are given in Figs. S5–S7 in the supporting information, and the barrier heights from these are given in Fig. 8e. The values for 1 and 2 dopant atoms were taken from the results described in Section 3.2. The GSFE barriers generally increase with the number of Al atoms, reaching about 75% of the barrier of bulk Ti at the highest concentration of Al studied. The system with 16 Al atoms, a snapshot of which is shown in Fig. 8c, is the only one with in which Al atoms were found to be in the M = 1 layer. The discussion in Section 3.1 supported the idea that having Al atoms in adjacent layers can destabilize some configurations with respect to others, increasing the GSFE barrier. This appears to be the case for the system with 16 Al atoms, which happens to have the highest GSFE barrier. Thus, two mechanisms have been identified for increasing GSFE barriers with dopants. One of them is destabilizing some configurations in which Al atoms are adjacent to one another, while the other is drawing electron density from the ceramic to stabilize the second Ti layer next to the nearest N layer. These two mechanisms appear to work in concert near the Ti/TiN barrier when 16 Al atoms are present, resulting in the largest increase in GSFE barriers.

4. Conclusion

The influence of doping on the shear resistance of Ti/TiN interfaces were studied with first principles density functional theory calculations. Al, V and Cr were separately examined as potential dopants, but Al was the only one that had a negative enthalpy of mixing in bulk Ti or Ti/TiN. For bulk Ti, the GSFE barrier height only increased when Al atoms were in adjacent layers to the slip plane. This coincided with the destabilizing effect of specific configurations in which Al atoms were in contact with one another. For undoped Ti/TiN, the N layer near the interface draws electron density away from the adjacent Ti layers in the Ti-phase weakening their interaction and GSFE barriers. The presence of Al atoms, which are more electronegative than Ti atoms, draws some of that electron density back into the Ti phase, leading to an enhancement of the slip resistance in the process. For higher doping concentrations, a Monte Carlo randomization scheme was used in conjunction with energy minimization to search for configurations with low energies. A general correlation between higher Al concentration and higher GSFE barriers was obtained. The higher barriers were attributed to a combination of more configurations with Al atoms in contact, in addition to Al atoms drawing some electron density from the ceramic into the Ti phase.

For coatings, there are often three components present: a substrate, often an iron alloy, the binding metal, and then the ceramic. For our particular work, only the interface between the binding metal and ceramic is considered. For scratch testing, it is difficult to elucidate the cause of delamination, as it could be related to the substrate/metal or metal/ceramic interface. In particular, the previous work that found TiAl/TiAlN to have a weaker critical load for delamination than Ti/TiN concluded that the origin of this was likely due to the lower lattice mismatch between substrate and Ti than TiAl [51]. Our work shows that most of the increase in shear resistance at the Ti/TiN interface can be realized with relatively low concentrations of Al. This suggests that a lower Al concentration than used in this previous work [51] that maintains matching between metal and substrate should further increase the critical load of delamination.

CRediT authorship contribution statement

Abu Shama Mohammad Miraz: Writing - Original draft, Investigation, Data curation, Formal analysis. **Eboni Williams:** Investigation. **W.J. Meng:** Funding acquisition, Conceptualization. **Bala R. Ramachandran:** Funding acquisition. **Collin D. Wick:** Supervision, Methodology, Writing - review & editing.

Declaration of Competing Interest

The authors declare that they have no known competing financial interests or personal relationships that could have appeared to influence the work reported in this paper.

Acknowledgement

The current work is funded by the US National Science Foundation under cooperative agreement #OIA-1541079.

Appendix A. Supplementary material

Supplementary data to this article can be found online at https://doi.org/10.1016/j.apsusc.2020.146185.

References

[1] J.S. Moya, S. Lopez-Esteban, C. Pecharromán, The challenge of ceramic/metal microcomposites and nanocomposites, Prog. Mater. Sci. 52 (2007) 1017–1090, https://doi.org/10.1016/j.pmatsci.2006.09.003.
[2] B. Cantor, F. Dunne, I. Stone, Institute of Physics (Great Britain), Oxford-Kobe Materials Seminar (3rd: 2000: Kobe Institute), Metal and ceramic matrix composites : an Oxford-Kobe materials text, 2004, pp. 429.
[3] N. Chawla, K.K. Chawla, Metal matrix composites, 2013. https://doi.org/10.1007/978-1-4614-9548-2.
[4] M. Taya, R.J. Arsenault, Metal matrix composites : thermomechanical behavior, Pergamon Press, 1989. https://www.sciencedirect.com/book/9780080369846/metal-matrix-composites#book-info (accessed February 18, 2019).
[5] H. Si Abdelkader, H.I. Faraoun, C. Esling, Effects of rhenium alloying on adhesion of Mo/HfC and Mo/ZrC interfaces: A first-principles study, J. Appl. Phys. 110 (2011), https://doi.org/10.1063/1.3624580.
[6] G. Feldbauer, M. Wolloch, P.O. Bedolla, J. Redinger, A. Vernes, P. Mohn, Suppression of material transfer at contacting surfaces: The effect of adsorbates on Al/TiN and Cu/diamond interfaces from first-principles calculations, J. Phys. Condens. Matter. 30 (2018), https://doi.org/10.1088/1361-648X/aaac91.
[7] N. Li, X.-Y. Liu, Review: mechanical behavior of metal/ceramic interfaces in nanolayered composites—experiments and modeling, J. Mater. Sci. 53 (2018) 5562–5583, https://doi.org/10.1007/s10853-017-1767-1.
[8] V. Bonu, M. Jeevitha, V. Praveen Kumar, H.C. Barshilia, Nanolayered multilayer Ti/TiN coatings: Role of bi-layer thickness and annealing on solid particle erosion behaviour at elevated temperature, Surf. Coat. Technol. 357 (2019) 204–211, https://doi.org/10.1016/j.surfcoat.2018.10.007.
[9] L. Rao, H. Liu, S. Liu, Z. Shi, X. Ren, Y. Zhou, Q. Yang, Interface relationship between TiN and Ti substrate by first-principles calculation, Comput. Mater. Sci. 155 (2018) 36–47, https://doi.org/10.1016/j.commatsci.2018.08.028.
[10] W. Yang, G. Ayoub, I. Salehinia, B. Mansoor, H. Zbib, The effect of layer thickness ratio on the plastic deformation mechanisms of nanoindented Ti/TiN nanolayered composite, Comput. Mater. Sci. 154 (2018) 488–498, https://doi.org/10.1016/j.commatsci.2018.08.021.
[11] W. Yang, G. Ayoub, I. Salehinia, B. Mansoor, H. Zbib, Deformation mechanisms in Ti/TiN multilayer under compressive loading, Acta Mater. 122 (2017) 99–108, https://doi.org/10.1016/j.actamat.2016.09.039.
[12] T. Sun, X. Wu, R. Wang, W. Li, Q. Liu, First-principles study on the adhesive properties of Al/TiC interfaces: Revisited, Comput. Mater. Sci. 126 (2017) 108–120, https://doi.org/10.1016/j.commatsci.2016.09.024.
[13] J. Horník, S. Krum, D. Tondl, M. Puchnin, P. Sachr, L. Cvrček, Multilayer coatings Ti/TiN, Cr/CrN AND W/WN deposited by magnetron sputtering for improvement of adhesion to base materials, Acta Polytech. 55 (2015) 388–392, https://doi.org/10.14311/AP.2015.55.0388.
[14] G. Pilania, B.J. Thijsse, R.G. Hoagland, I. LaziÄ, S.M. Valone, X.Y. Liu, Revisiting the Al/Al 2 O 3 interface: Coherent interfaces and misfit accommodation, Sci. Rep. 4 (2014) 1–9, https://doi.org/10.1038/srep04485.
[15] S.K. Yadav, R. Ramprasad, J. Wang, A. Misra, X.Y. Liu, First-principles study of Cu/TiN and Al/TiN interfaces: Weak versus strong interfaces, Model. Simul. Mater. Sci. Eng. 22 (2014), https://doi.org/10.1088/0965-0393/22/3/035020.
[16] D.H.R. Fors, G. Wahnström, Theoretical study of interface structure and energetics in semicoherent Fe(001)/MX(001) systems (M = Sc, Ti, V, Cr, Zr, Nb, Hf, Ta; X = C or N), Phys. Rev. B - Condens. Matter Mater. Phys. 82 (2010) 1–13, https://doi.org/

10.1103/PhysRevB.82.195410.
[17] M. Damadam, S. Shao, I. Salehinia, G. Ayoub, H.M. Zbib, Molecular dynamics simulations of mechanical behavior in nanoscale ceramic–metallic multilayer composites, Mater. Res. Lett. 5 (2017) 306–313, https://doi.org/10.1080/21663831.2016.1275864.
[18] M. Damadam, S. Shao, G. Ayoub, H.M. Zbib, Recent advances in modeling of interfaces and mechanical behavior of multilayer metallic/ceramic composites, J. Mater. Sci. 53 (2018) 5604–5617, https://doi.org/10.1007/s10853-017-1704-3.
[19] I. Salehinia, S. Shao, J. Wang, H.M. Zbib, Interface structure and the inception of plasticity in Nb/NbC nanolayered composites, Acta Mater. 86 (2015) 331–340, https://doi.org/10.1016/j.actamat.2014.12.026.
[20] X. Guo, Y. Zhang, Y.-G. Jung, L. Li, J. Knapp, J. Zhang, Ideal tensile strength and shear strength of ZrO2(111)/Ni(111) ceramic-metal Interface: A first principle study, Mater. Des. 112 (2016) 254–262, https://doi.org/10.1016/j.matdes.2016.09.073.
[21] A. Sazgar, M.R. Movahhedy, M. Mahnama, S. Sohrabpour, A molecular dynamics study of bond strength and interface conditions in the Al/Al2O3 metal-ceramic composites, Comput. Mater. Sci. 109 (2015) 200–208, https://doi.org/10.1016/j.commatsci.2015.07.024.
[22] L. Chen, J. Paulitsch, Y. Du, P.H. Mayrhofer, Thermal stability and oxidation resistance of Ti-Al-N coatings, Surf. Coat. Technol. 206 (2012) 2954–2960, https://doi.org/10.1016/j.surfcoat.2011.12.028.
[23] S.C.D.S. PalDey, S.C. Deevi, Single layer and multilayer wear resistant coatings of (Ti, Al)N: A review, Mater. Sci. Eng. A 342 (2003) 58–79, https://doi.org/10.1016/S0921-5093(02)00259-9.
[24] A.R. Shugurov, M.S. Kazachenok, Mechanical properties and tribological behavior of magnetron sputtered TiAlN/TiAl multilayer coatings, Surf. Coat. Technol. 353 (2018) 254–262, https://doi.org/10.1016/j.surfcoat.2018.09.001.
[25] M.T. Vieira, A.S. Ramos, Influence of ductile interlayers on the mechanical performance of tungsten nitride coatings, J. Mater. Process. Technol. 92–93 (1999) 156–161, https://doi.org/10.1016/S0924-0136(99)00235-6.
[26] J.M. Lackner, L. Major, M. Kot, Microscale interpretation of tribological phenomena in Ti/TiN soft-hard multilayer coatings on soft austenite steel substrates, Bull. Polish Acad. Sci. Tech. Sci. 59 (2011) 343–356, https://doi.org/10.2478/v10175-011-0042-x.
[27] W. Tillmann, E. Vogli, S. Momeni, Mechanical and tribological properties of Ti/TiAlN duplex coatings on high and low alloy tool steels, Vacuum 84 (2009) 387–392, https://doi.org/10.1016/j.vacuum.2009.08.001.
[28] E. Vogli, W. Tillmann, U. Selvadurai-Lassl, G. Fischer, J. Herper, Influence of Ti/TiAlN-multilayer designs on their residual stresses and mechanical properties, Appl. Surf. Sci. 257 (2011) 8550–8557, https://doi.org/10.1016/j.apsusc.2011.05.013.
[29] D. Ham, J. Lee, Transition metal carbides and nitrides as electrode materials for low temperature fuel cells, Energies 2 (2009) 873–899, https://doi.org/10.3390/en20400873.
[30] M. Halbig, M. Jaskowiak, J. Kiser, D. Zhu, Evaluation of ceramic matrix composite technology for aircraft turbine engine applications, in: 51st AIAA Aerosp. Sci. Meet. Incl. New Horizons Forum Aerosp. Expo., American Institute of Aeronautics and Astronautics, Reston, Virigina, 2013. https://doi.org/10.2514/6.2013-539.
[31] N.D. Nam, M.J. Kim, D.S. Jo, J.G. Kim, D.H. Yoon, Corrosion protection of Ti/TiN, Cr/TiN, Ti/CrN, and Cr/CrN multi-coatings in simulated proton exchange membrane fuel cell environment, Thin Solid Films 545 (2013) 380–384, https://doi.org/10.1016/j.tsf.2013.07.056.
[32] A. Vereschaka, S. Grigoriev, N. Sitnikov, G. Oganyan, C. Sotova, Influence of thickness of multilayer composite nano-structured coating Ti-TiN- (Ti, Al, Cr) N on tool life of metal-cutting tool, Proc. CIRP (2018) 4–7, https://doi.org/10.1016/j.procir.2018.08.237.
[33] A. Vereschaka, E. Kataeva, N. Sitnikov, A. Aksenenko, G. Oganyan, C. Sotova, Influence of thickness of multilayered nano-structured coatings Ti-TiN-(TiCrAl)N and Zr-ZrN-(ZrCrNbAl)N on tool life of metal cutting tools at various cutting speeds, Coatings 8 (2018) 1–9, https://doi.org/10.3390/coatings8010044.
[34] J.C. Jiang, W.J. Meng, A.G. Evans, C.V. Cooper, Structure and mechanics of W-DLC coated spur gears, Surf. Coat. Technol. 176 (2003) 50–56, https://doi.org/10.1016/S0257-8972(03)00445-6.
[35] M.N. Kotzalas, G.L. Doll, Tribological advancements for reliable wind turbine performance, Philos. Trans. R. Soc. A Math. Phys. Eng. Sci. 368 (2010) 4829–4850, https://doi.org/10.1098/rsta.2010.0194.
[36] G.M. Robinson, M.J. Jackson, M.D. Whitfield, A review of machining theory and tool wear with a view to developing micro and nano machining processes, J. Mater. Sci. 42 (2007) 2002–2015, https://doi.org/10.1007/s10853-006-0171-z.
[37] E.A. Jarvis, E.A. Carter, Importance of open-shell effects in adhesion at metal-ceramic interfaces, Phys. Rev. B - Condens. Matter Mater. Phys. 66 (2002) 1001031–1001034, https://doi.org/10.1103/PhysRevB.66.100103.
[38] E.A.A. Jarvis, E.A. Carter, An atomic perspective of a doped metal-oxide interface, J. Phys. Chem. B 106 (2002) 7995–8004, https://doi.org/10.1021/jp0257348.
[39] H.Z. Zhang, S.Q. Wang, The effects of Zn and Mg on the mechanical properties of the Al/TiN interface: A first-principles study, J. Phys. Condens. Matter. 19 (2007), https://doi.org/10.1088/0953-8984/19/22/226003.
[40] T. Sun, X. Wu, W. Li, R. Wang, The mechanical and electronic properties of Al/TiC interfaces alloyed by Mg, Zn, Cu, Fe and Ti: First-principles study, Phys. Scr. 90 (2015), https://doi.org/10.1088/0031-8949/90/3/035701.
[41] S. Choudhury, J.A. Aguiar, M.J. Fluss, L.L. Hsiung, A. Misra, B.P. Uberuaga, Non-uniform solute segregation at semi-coherent metal/oxide interfaces, Sci. Rep. 5 (2015) 1–9, https://doi.org/10.1038/srep13086.
[42] H. Xiong, H. Zhang, H. Zhang, Y. Zhou, Effects of alloying elements X (X = Zr, V, Cr, Mn, Mo, W, Nb, Y) on ferrite/TiC heterogeneous nucleation interface: first-principles study, J. Iron Steel Res. Int. 24 (2017) 328–334, https://doi.org/10.1016/S1006-706X(17)30047-X.
[43] Y. Lin, Y. Cai, E. Drioli, Y. Fan, Enhancing mechanical and photocatalytic performances on TiO2/Ti composite ultrafiltration membranes via Ag doping method, Sep. Purif. Technol. 145 (2015) 29–38, https://doi.org/10.1016/j.seppur.2015.02.024.
[44] Z.G. Liu, C.Y. Wang, T. Yu, Influence of Re on the propagation of a Ni/Ni3Al interface crack by molecular dynamics simulation, Model. Simul. Mater. Sci. Eng. 21 (2013), https://doi.org/10.1088/0965-0393/21/4/045009.
[45] L. Peng, P. Peng, D.D. Wen, Y.G. Liu, H. Wei, X.F. Sun, Z.Q. Hu, Site preference of S-doping and its influence on the properties of a Ni/Ni3Al interface, Model. Simul. Mater. Sci. Eng. 19 (2011), https://doi.org/10.1088/0965-0393/19/6/065002.
[46] Y.X. Wu, X.Y. Li, Y.M. Wang, First-principles study of the influence of lattice misfit on the segregation behaviors of hydrogen and boron in the Ni-Ni3Al system, Acta Mater. 55 (2007) 4845–4852, https://doi.org/10.1016/j.actamat.2007.05.006.
[47] M. Wessel, N.V. Skorodumova, M. Wessel, N.V. Skorodumova, Adhesion of the TiN/Fe interface with point defects from first principles, J. Appl. Phys. (2016) 14905, https://doi.org/10.1063/1.4772756.
[48] G. Elssner, D. Korn, M. Rühle, The influence of interface impurities on fracture energy of UHV diffusion bonded metal-ceramic bicrystals, Scr. Metall. Mater. 31 (1994) 1037–1042, https://doi.org/10.1016/0956-716X(94)90523-1.
[49] W.G. Sloof, I.J. Bennett, Modelling the influence of reactive elements on the work of adhesion between a thermally grown oxide and a bond coat alloy, Mater. Corros. 57 (2006) 223–229, https://doi.org/10.1002/maco.200503928.
[50] I.J. Bennett, J.M. Kranenburg, W.G. Sloof, Modeling the influence of reactive elements on the work of adhesion between oxides and metal alloys, J. Am. Ceram. Soc. 88 (2005) 2209–2216, https://doi.org/10.1111/j.1551-2916.2005.00408.x.
[51] D.A. Colombo, A.D. Mandri, M.D. Echeverría, J.M. Massone, R.C. Dommarco, Mechanical and tribological behavior of Ti/TiN and TiAl/TiAlN coated austempered ductile iron, Thin Solid Films 647 (2018) 19–25, https://doi.org/10.1016/j.tsf.2017.12.014.
[52] M.A. Al-Bukhaiti, K.A. Al-Hatab, W. Tillmann, F. Hoffmann, T. Sprute, Tribological and mechanical properties of Ti/TiAlN/TiAlCN nanoscale multilayer PVD coatings deposited on AISI H11 hot work tool steel, Appl. Surf. Sci. 318 (2014) 180–190, https://doi.org/10.1016/j.apsusc.2014.03.026.
[53] L. Ipaz, J.C. Caicedo, J. Esteve, F.J. Espinoza-Beltran, G. Zambrano, Improvement of mechanical and tribological properties in steel surfaces by using titanium-aluminum/titanium-aluminum nitride multilayered system, Appl. Surf. Sci. 258 (2012) 3805–3814, https://doi.org/10.1016/j.apsusc.2011.12.033.
[54] X. Zhang, B. Zhang, Y. Mu, S. Shao, C.D. Wick, B.R. Ramachandran, W.J. Meng, Mechanical failure of metal/ceramic interfacial regions under shear loading, Acta Mater. 138 (2017) 224–236, https://doi.org/10.1016/j.actamat.2017.07.053.
[55] A.S.M. Miraz, S. Sun, S. Shao, W.J. Meng, B.R. Ramachandran, C.D. Wick, Computational study of metal/ceramic interfacial adhesion and barriers to shear displacement, Comput. Mater. Sci. 168 (2019) 104–115, https://doi.org/10.1016/j.commatsci.2019.06.006.
[56] J.P. Perdew, K. Burke, M. Ernzerhof, Generalized gradient approximation made simple, Phys. Rev. Lett. 77 (1996) 3865–3868, https://doi.org/10.1103/PhysRevLett.77.3865.
[57] G. Kresse, J. Furthmüller, Efficient iterative schemes for ab initio total-energy calculations using a plane-wave basis set, Phys. Rev. B - Condens. Matter Mater. Phys. 54 (1996) 11169–11186.
[58] J. Hafner, Ab-initio simulations of materials using VASP: Density-functional theory and beyond, J. Comput. Chem. 29 (2008) 2044–2078, https://doi.org/10.1002/jcc.21057.
[59] H.J. Monkhorst, J.D. Pack, Special points for Brillouin-zone integrations, Phys. Rev. B. 13 (1976) 5188–5192, https://doi.org/10.1103/PhysRevB.13.5188.
[60] Y.H. Cheng, T. Browne, B. Heckerman, J.C. Jiang, E.I. Meletis, C. Bowman, V. Gorokhovsky, Internal stresses in TiN/Ti multilayer coatings deposited by large area filtered arc deposition, J. Appl. Phys. 104 (2008) 93502, https://doi.org/10.1063/1.3006136.
[61] C. Sant, M. Ben Daia, P. Aubert, S. Labdi, P. Houdy, Interface effect on tribological properties of titanium–titanium nitride nanolaminated structures, Surf. Coat. Technol. 127 (2000) 167–173, https://doi.org/10.1016/S0257-8972(00)00663-0.
[62] C. Leyens, M. Peters (Eds.), Titanium and Titanium Alloys, Wiley, Weinheim, FRG, 2003, , https://doi.org/10.1002/3527602119.
[63] G. Lütjering, J.C. Williams, A. Gysler, Microstructure and mechanical properties of titanium alloys, Microstruct. Prop. Mater. World Scientific, 2000, pp. 1–77, , https://doi.org/10.1142/9789812793959_0001.
[64] A.S. Mohammad Miraz, S. Sun, S. Shao, W.J. Meng, B.R. Ramachandran, C.D. Wick, Computational study of metal/ceramic interfacial adhesion and barriers to shear displacement, Comput. Mater. Sci. 168 (2019) 104–115, https://doi.org/10.1016/j.commatsci.2019.06.006.
[65] W. Tang, E. Sanville, G. Henkelman, A grid-based Bader analysis algorithm without lattice bias, J. Phys. Condens. Matter. 21 (2009) 84204, https://doi.org/10.1088/0953-8984/21/8/084204.
[66] G. Henkelman, A. Arnaldsson, H. Jónsson, A fast and robust algorithm for Bader decomposition of charge density, Comput. Mater. Sci. 36 (2006) 354–360, https://doi.org/10.1016/j.commatsci.2005.04.010.
[67] A.L. Allred, Electronegativity values from thermochemical data, J. Inorg. Nucl. Chem. 17 (1961) 215–221, https://doi.org/10.1016/0022-1902(61)80142-5.
[68] C. Leyens, M. Peters (Eds.), Titanium and Titanium Alloys, Wiley, 2003, , https://doi.org/10.1002/3527602119.
[69] S. Djanarthany, J.-C. Viala, J. Bouix, An overview of monolithic titanium aluminides based on Ti3Al and TiAl, Mater. Chem. Phys. 72 (2001) 301–319, https://doi.org/10.1016/S0254-0584(01)00328-5.